Materials Horizons

ROYAL SOCIETY OF CHEMISTRY

COMMUNICATION

View Article Online
View Journal

Check for updates

Cite this: DOI: 10.1039/d5mh00698h

Received 14th April 2025,
Accepted 19th June 2025

DOI: 10.1039/d5mh00698h

rsc.li/materials-horizons

Enhanced selective gold recovery from e-waste *via* synergistic hetero-atom controlled quasi-planar benzoxazine-based covalent organic frameworks†

Sushil Kumar, ‡[ae] Mahira Bashri,‡[a] Safa Gaber, [a] José I. Martínez, [b]
Matthew J. O'Connor,[c] Sabu Varghese,[c] Blaž Belec,[d] Gisha Elizabeth Luckachan[a]
and Dinesh Shetty *[ae]

Efficient and selective gold recycling from e-waste mixtures is crucial for advancing sustainability, the circular economy, and waste management objectives. However, the complex composition of e-waste and the underdeveloped practical potential of current adsorbents highlight the need for innovative sorbent development. Here, we present quasi-planar, benzoxazine-core-based two-dimensional covalent organic frameworks (COFs) with synergistic hetero-atom control across the network, achieved *via* a multi-component synthetic approach. These COFs, designed with specific gold interaction sites, were explored for the highly selective recovery of gold from real e-waste mixtures. By tuning the hetero-atom distribution, we achieved an impressive gold uptake capacity of 3467 mg g^{-1} and over 92% selectivity in presence of 12 competing metal ions from e-waste leachate. These findings underscore the critical role of molecular-level engineering in COF sorbents, paving the way for the practical recovery of noble metals from e-waste.

New concepts

Selective and efficient gold reclamation from e-waste mixtures is paramount for fostering sustainability, circular economy principles, and optimized waste management strategies. The heterogeneous nature of e-waste and the limited efficacy of existing adsorbents underscore the demand for advanced sorbent innovation. To address this, we introduce two new quasi-planar benzoxazine-core-derived two-dimensional covalent organic frameworks (COFs) with integrated heteroatoms, crafted through a multi-component synthetic methodology. Tailored with precise gold-binding domains, these COFs—namely PGBpy and PGBD—incorporate N_{amine}, N_{Bpy}, and O_{ether} linkages, enabling highly selective gold extraction from authentic e-waste samples. This strategic design yielded remarkable gold uptake capacities of 3467 mg g^{-1} (PGBpy) and 2590 mg g^{-1} (PGBD), driven by the critical influence of embedded N_{amine} and O_{ether} heteroatoms within the COF structure, which preferentially sequester gold ions amidst competing metal ions in acidic leachates. Both COFs exhibited over 92% gold selectivity, retaining stability and porosity, with DFT analyses confirming the pivotal role of heteroatoms in the benzoxazine core and auxiliary Bpy unit in amplifying adsorption selectivity and efficiency.

1. Introduction

Today's world is witnessing an overwhelming presence of electronic devices across every sector of daily life, resulting in a corresponding increase in the volume of electronic waste (e-waste). According to the Global E-waste Monitor 2024 report, 62 billion kg of global e-waste was generated in 2022; however, only 13.8 billion kg of this e-waste was collected and recycled.[1] This disparity has created an alarming situation that demands urgent global attention. The report further indicates that 50% of the worldwide e-waste was metal-based, including valuable precious metals. Gold, particularly, is highly prized for its economic value and exceptional chemical stability. It is crucial in various industries, including pharmaceuticals,[2,3] energy storage,[4] catalysis,[5,6] and electronics.[7,8] Typically, e-waste generated from printed circuit boards consists of approximately 40–50% metals, while the rest are plastic and ceramics. Gold concentration in e-waste can range from 3–30 gt^{-1}, significantly greater than raw-grade ore.[9] However, many competing metal ions are often present within e-waste, which can easily alter the selective recovery of gold from e-waste. In addition to this, before the recovery process, the plastic and ceramics were removed from e-waste using toxic organic solvents. Thus, it is a formidable challenge to recover the gold selectively from

---

[a] Department of Chemistry, Khalifa University of Science & Technology, Abu Dhabi, 127788, United Arab Emirates. E-mail: dinesh.shetty@ku.ac.ae
[b] Instituto de Ciencia de Materiales de Madrid (ICMM-CSIC), C/Sor Juana Inés de la Cruz 3, 28049, Madrid, Spain
[c] Core Technology Platform, New York University Abu Dhabi (NYUAD), Saadiyat Island, 129188, Abu Dhabi, United Arab Emirates
[d] Materials Research Laboratory, University of Nova Gorica, Vipavska 11c, Slovenia
[e] Center for Catalysis & Separations (CeCaS), Khalifa University of Science & Technology, Abu Dhabi, 127788, United Arab Emirates

† Electronic supplementary information (ESI) available. See DOI: https://doi.org/10.1039/d5mh00698h

‡ These authors contributed equally.

e-waste sustainably. There are several methods developed for gold recovery, including hydrometallurgical,[10] incineration,[11] smelting,[12] adsorption,[13] chemical precipitation,[14] solvent extraction,[15] and ion exchange.[10,16,17] Among them, the adsorption technique is the most dependable because of its ease of operation, high efficacy, economic, and reuse potential. There have been various gold adsorbents explored, however, the limited adsorption capacity, sluggish kinetics, inadequate selectivity, and complex desorption limit their usefulness in gold recovery.[18–20] Therefore, developing a highly effective adsorbent with superior selectivity, a considerable adsorption capacity, and significant chemical durability is essential for real-life translation.

Covalent organic frameworks (COFs) are organized structures of organic units linked by covalent bonds,[21] offering great adsorption potential due to their intrinsic porosity, exceptional durability, and regenerative nature.[13,22] COFs synthesis allows precise control over pore structure and chemical characteristics through reticular and dynamic covalent chemistry.[21] However, few studies explore COFs for gold recovery from e-waste, where the pore interior functionalized with groups such as –SH, $-NH_2$, and –OH to enhance molecular interactions.[23,24] Multicomponent synthesis is a useful strategy where we can introduce multiple metal coordination sites decorated pore interiors to improve interactions with the adsorbed species.[25]

The role of the quasi-planar core containing COF skeleton in a heteroatomic pore environment is an interesting avenue of research. Benzoxazine-containing polymers exhibit high thermal stability,[26,27] excellent electronic properties, and strong chemical stability.[28,29] While one-dimensional COF featuring quasi-conjugated chains with a benzoxazine-core has recently been reported.[30] To the best of our knowledge, a quasi-planar benzoxazine-core-based two-dimensional (2D) COFs have not yet been reported in the literature. We envision that 2D benzoxazine-core COFs, combined with a synergistically heteroatom-controlled backbone and enhanced stability, could be promising candidates for recovering precious metals from e-waste. Considering these facts, we synthesized two such COFs *i.e.* PGBpy and PGBD, with active gold-interaction pockets having N_{amine}, N_{Bpy}, and O_{ether} linkages *via* multi-component synthesis. The rational design resulted in efficient recovery of gold from e-waste, contributing to a high uptake value of 3467 mg g^{-1} for gold ions with PGBpy and 2590 mg g^{-1} with PGBD. The obtained results highlight the importance of inherited heteroatoms *i.e.* N_{amine} atoms and O_{ether} atoms within the COF backbone in facilitating the selective capture of gold ions in the presence of other competing metal ions present in e-waste leach solution. Both COFs displayed >92% selectivity for gold under acidic conditions, even in real e-waste, without compromising its stability and porosity. DFT studies corroborated the crucial role of heteroatoms in the benzoxazine-core

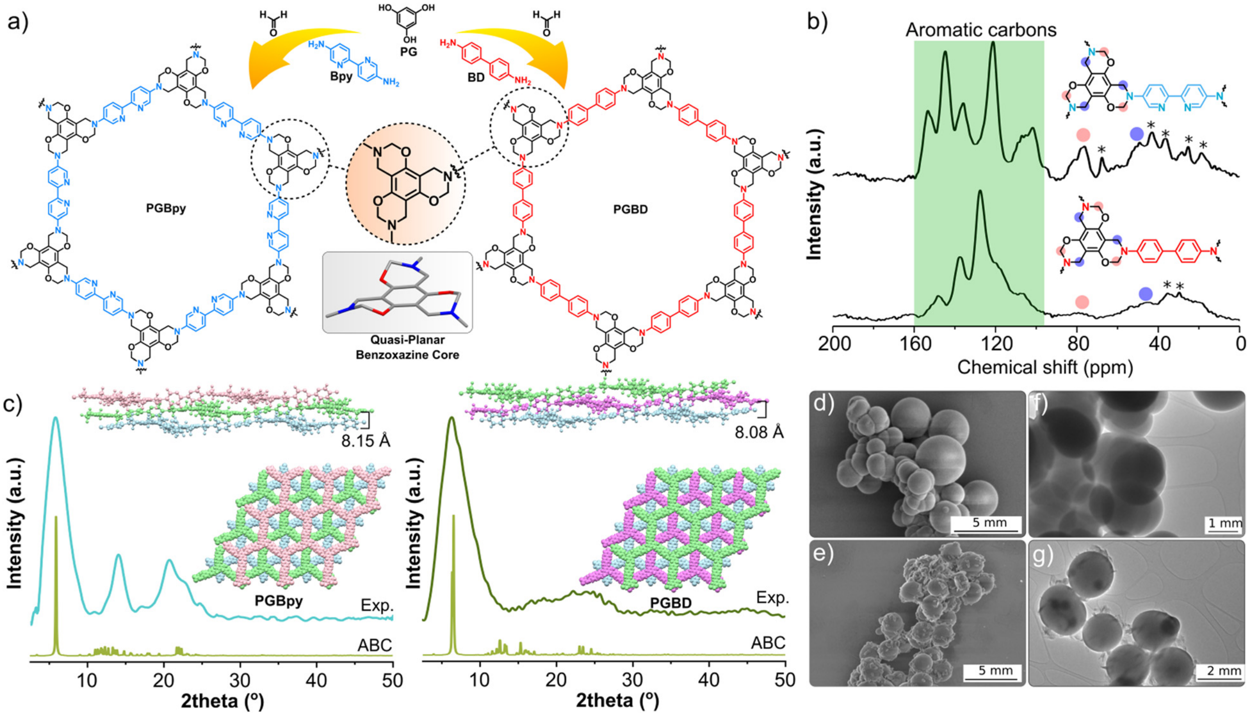

Fig. 1 (a) Synthesis and chemical structure of PGBpy and PGBD. (b) Solid state ^{13}C CP-MAS NMR confirms the formation of quasi-planar benzoxazine core in PGBpy and PGBD COFs, where asterisk represents the spinning side bands and trapped oligomers formed during synthesis. (c) After Pawley refinement, the individual comparison of the experimental PXRD pattern with the one generated from their respective simulated ABC model shows good agreement with each other; PGBpy (R_p 4.22%), and PGBD (R_p 2.17%). SEM images of (d) PGBpy and (e) PGBD show spherical morphology. TEM images of (f) PGBpy and (g) PGBD further confirm the spherical morphology.

and supplementary Bpy unit in enhancing selectivity and adsorption efficiency.

2. Experimental

2.1 Materials and methods

Detailed descriptions of the materials and reagents, synthesis, characterizations, gold adsorption, calculations, e-waste preparation, and theoretical studies details are provided in the ESI.†

3. Results and discussion

3.1 COFs synthesis and characterizations

Quasi-planar benzoxazine core-based PGBpy and PGBD were synthesized *via* solvothermal condensation (Fig. 1a), using phloroglucinol (PG), bipyridine diamine (Bpy) or benzidine (BD), and aqueous formaldehyde (37%), with glacial acetic acid as a catalyst in ethanol. After sonication for 30 minutes, the mixture was heated at 100 °C for 12 h under an inert atmosphere, yielding 60–70% with varied hetero-atom distribution. The COFs were purified using Soxhlet extraction with methanol and THF (Section S2, ESI†). PGBpy and PGBD were first characterized *via* FTIR spectroscopy to understand the formation of the benzoxazine core between the corresponding organic linkers (Section S4, ESI†). A –C=C– stretching band for the aromatic group was present at 1592 cm^{-1}. Notably, the C–O stretch present in PG moiety was found to be shifted from 1294 cm^{-1} to 1256 cm^{-1} in as-synthesized COFs, suggesting the formation of a $C–O_{ether}$ bond. Similarly, the N–H stretch of the amine group present in the Bpy or BD disappeared, suggesting the formation of the C–N bond and no contamination from the starting material. The formation of a benzoxazine core was further verified by solid-state ^{13}C CP-MAS NMR studies (Fig. 1b). The peak present at 76 ppm (for PGBpy) and 79 ppm (for PGBD) corresponds to the $–CH_2–O–$ bonds, whereas the peaks present at 49 ppm (for PGBpy) and 53 ppm (for PGBD) are assigned to the $–CH_2–N–$ bonds, which suggests the successful formation of benzoxazine core containing framework. Aromatic carbons were found to resonate in the 100–160 ppm range.

The crystallinity of PGBpy and PGBD were elucidated using powder X-ray diffraction (PXRD) analysis (Fig. 1c). PXRD pattern displayed a first peak at $2\theta = 5.78°$ (PGBpy) and 5.92° (PGBD), corresponding to diffraction from 110 facets, with a second peak at $2\theta = 14°$ for diffraction from 101 facets. However, in the case of PGBD, the second peak is broad and, thus, difficult to locate precisely. For both COFs, a broad peak in the range $2\theta = 18–25°$ corresponds to diffraction from 002 facets. Three stacking models were computationally simulated to delineate the framework structure of PGBpy and PGBD, and the corresponding model's PXRD patterns were generated and compared with the experimental PXRD pattern (Fig. S3, ESI†). According to our analysis, the theoretical PXRD patterns for the eclipsed AA and staggered AB stacking models exhibit their first diffraction peaks at approximately $2\theta = 3.56°$, which significantly deviate from the experimental first peak positions observed for PGBpy and PGBD. This mismatch indicates that neither the AA nor AB stacking models accurately represent the structural arrangement of our COFs. Attempting Pawley refinement against these models would indeed yield high R and R_{wp} values, rendering such refinements uninformative due to the poor fit between theoretical and experimental data. In contrast, the PXRD pattern simulated for the ABC stacking model matches well with experimental PXRD pattern, as illustrated in Fig. 1c. This suggests that the ABC stacking configuration better approximates the actual framework structure. Pawley refinement performed for both COFs resulted in the following fitting parameters: for PGBpy: $R_{wp} = 3.98\%$ and $R_p = 4.22\%$, and for PGBD: $R_{wp} = 2.94\%$ and $R_p = 2.17\%$. Following Pawley refinement, the unit cell dimensions were derived as follows: for PGBpy: $a = 30.10$ Å, $b = 30.04$ Å, and $c = 8.15$ Å; $\alpha = 92.57°$, $\beta = 92.44°$, and $\gamma = 120.67°$; and for PGBD: $a = 30.18$ Å, $b = 29.67$ Å, and $c = 8.08$ Å; $\alpha = 81.43°$, $\beta = 84.38°$, and $\gamma = 119.79°$ (Sections S5 and S6, ESI†). Notably, the closeness in magnitude between parameters a and b, alongside the proximity of the angle between a and b to 120°, suggests a two-dimensional hexagonal lattice arrangement within each layer. This observation suggests the formation of an ordered hexagonal porous structure within PGBpy and PGBD. The high value of R_{wp} (w/o bck) observed in the PXRD pattern generated after performing the Pawley refinement for the ABC model indicates moderate crystallinity (Fig. S4 and S5, ESI†). Nevertheless, we would like to emphasize that the primary goal of our design is not to achieve maximal crystallinity or porosity but rather to exploit the unique properties of the benzoxazine core—namely its flexibility and heteroatom-rich composition—for enhanced metal ion adsorption.

To determine the morphology of these COFs, scanning electron microscopy (SEM) and transmission electron microscopy (TEM) images were collected. The SEM images of PGBpy and PGBD show spherical morphology with average sizes of 2.5 and 2.0 μm (Fig. 1d and e, respectively). TEM images further confirm the spherical morphology (Fig. 1f and g). In the case of PGBD, some sheet-like structure is attached to the sphere surface, as observed in its TEM (Fig. 1g). These sheets were most probably generated *via* exfoliation of the surface of the sphere or breakdown of the small sphere during the sonication process employed in sample preparation for SEM/TEM studies. A similar observation is also noticed in PGBpy, where small spheres and sheets are present on a very small scale (Fig. S12, Section S7, ESI†). The chemical structure was further surveyed by XPS analysis (Section S8, ESI†). Both COFs displayed three intense peaks in the spectra, representing C 1s, N 1s, and O 1s signals. In the deconvoluted XPS profile of C 1s, the two signals present at 283.28 and 284.26 eV (for PGBpy), 283.38 and 284.47 eV (for PGBD) are assigned to C=C and C–C bonds, respectively, present in the framework (Section S8, ESI†). The broad signal at 285.64 eV (for PGBpy) and 286.34 eV (for PGBD) was assigned to the C–O or C–N bond. The high-resolution N 1s spectra displayed two signals at 398.77 eV (for PGBpy) and 398.82 eV (PGBD), corresponding to the C–N bond formed during the condensation reaction (Section S8, ESI†). In contrast, the signal at 397.81 eV corresponded to the C═N bond of the Bpy unit. Moreover, in the high-resolution spectra of O 1s, the signals present at 531.80 and 533.18 eV (PGBpy); and 530.84 and 532.71 eV (PGBD) are attributed to the C–O–C and adventitious C–OH bond, respectively (Section S8, ESI†). Based on the above analysis, we conclude the formation of the benzoxazine core in the PGBpy and PGBD, along with some unreacted hydroxyl groups within the framework structures.

The porous nature of PGBpy and PGBD, crucial for metal ion adsorption from e-waste was analyzed *via* nitrogen gas sorption isotherm, revealing a type II isotherm. The BET surface area (SBET) values were 1557 m^2 g^{-1} (PGBpy) and 931 m^2 g^{-1} (PGBD), with mesoporous pore sizes of 28–58 Å (PGBpy) and 28–60 Å (PGBD) (Section S9, ESI†). The pore sizes align with the simulated COF, but larger-than-expected values suggest structural defects or partial layer offset, possibly due to the benzoxazine core's flexibility, which may disrupt ideal ABC stacking and from mesoporous channel.[31] The BET isotherms and PXRD patterns, showing a decent surface area and broader peaks respectively, suggest reduced crystallinity and deviate from the conventional advantages of planar COFs, where strong interlayer π–π stacking typically enhances porosity and structural order. The chemical stability of both COFs was investigated under acidic and basic conditions. FTIR spectra of PGBpy after 3 M hydrochloric acid treatment showed no significant shift in the characteristic stretching bands (Section S11, ESI†), while treatment with 3 M NaOH led to the disappearance of characteristic C═C and C–N peaks, suggesting framework disintegration. Similar observation was noticed in PXRD studies (Fig. S21, ESI†). It is important to note that the intended application of the developed COFs is to selectively recover gold from e-waste leachate, which is generally acidic in nature, and, therefore, the lack of stability in the basic conditions is less of a concern.

3.2 Gold adsorption studies

The benzoxazine moiety was strategically integrated into the COF skeleton to functionalize the pore interior for metal ion coordination. These quasi-planar COFs are, though modestly porous and weakly crystalline, enhance selective interactions between heteroatom-lined pores and metal ions while benzoxazine core's flexibility enables a dynamic pore environment aiding adaptive binding to metal ions of different sizes and charges, supporting our gold adsorption goals. To explore the potential of benzoxazine-core based-COFs consisting of active metal interaction pockets containing polar hetero atoms for the selective recovery of gold, the uptake potential of these COFs was investigated by constant shaking (100 rpm) with a definite amount of COF in aqueous $AuCl_3$ solutions at room temperature. The gradual gold adsorption efficiencies were monitored by injecting filtrate samples into an inductively coupled plasma mass spectrometer (ICP-MS). Detailed procedures and calculations performed for each study are provided in Section S3 (ESI†). The gold adsorption kinetics of COFs was investigated by monitoring the adsorption efficiency with respect to time

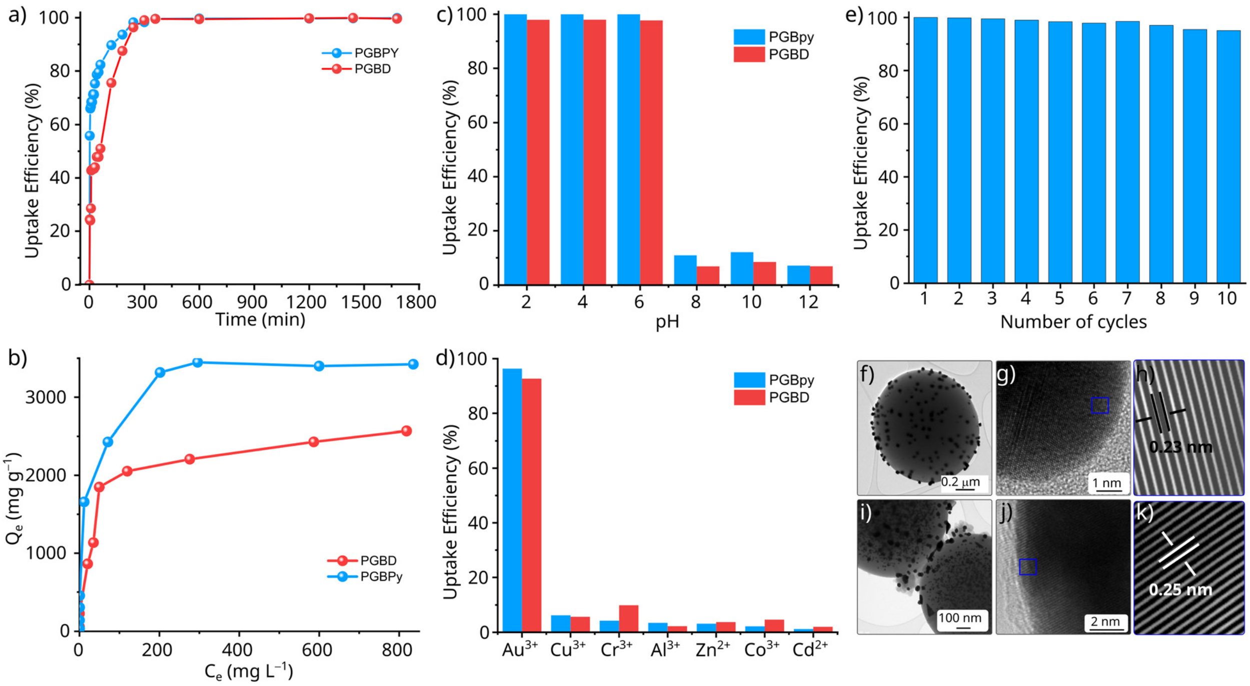

Fig. 2 (a) The gold uptake efficiencies of PGBpy and PGBD with time, (b) Q_e *versus* C_e plot for PGBpy and PGBD for various initial gold concentrations, (c) uptake efficiencies of PGBpy and PGBD ranging from acidic to alkaline pH, (d) selective uptake of gold ions with respect to competing ions for PGBD and PGBpy, (e) uptake efficiencies of gold ions after each regeneration cycles for PGBpy, (f) TEM image of Au@PGBpy, (g) TEM image of one gold nanoparticle, (h) fringe width image, (i) TEM image of Au@PGBD, (j) TEM image of a gold nanoparticle, and (k) fringe width image (inset).

(Fig. 2a). Compared to PGBD, the kinetic of PGBpy was higher due to the presence of supplementary Bpy units with pyridyl nitrogen (N_{Bpy}) sites and the benzoxazine core. Within 30 h, a quantitative uptake of Au ions was observed for both PGBpy and PGBD. Both COFs exhibited an uptake efficiency value of >99.9% at equilibrium time. To determine whether the adsorption mechanism of Au^{3+} ions onto PGBpy potentially involves physisorption or chemisorption pathways, the kinetic data points obtained for these COFs were best fitted using a pseudo-second-order kinetic model (Fig. S25a and S26a, ESI†). The R^2 values of PGBpy and PGBD were calculated as 0.9999 and 0.9996, respectively, with a rate constant (k_2) value of 1.4930×10^{-4} g mg^{-1} min^{-1} and 4.738×10^{-5} g mg^{-1} min^{-1}, respectively. Meanwhile, the first-order kinetic model displayed R^2 values of 0.9809 and 0.9735 for PGBpy and PGBD, respectively, clearly suggesting the non-suitability of the model to understand the adsorption behavior (Fig. S25b and S26b, ESI†).

The equilibrium gold adsorption capacities (Q_e) of benzoxazine-core based-COFs were obtained by adsorbing aqueous $AuCl_3$ solutions with varied initial concentrations (C_i) ranging from 1 to ~2000 mg L^{-1} (Fig. 2b). The adsorption capacities obtained were fitted with the Langmuir and Freundlich adsorption isotherm models (Fig. S27 and S28, ESI†). The adsorption isotherms exhibited a strong correlation with the Langmuir model (R^2 >0.998, for PGBpy; and >0.995, for PGBD) compared to the Freundlich model (R^2 >0.876, for PGBpy; and >0.914, for PGBD), suggesting the strong monolayer adsorption of Au ions over COF skeleton. In our study, the adsorption isotherms for Au (likely as $[AuCl_4]^-$ ions before reduction) strongly fit the Langmuir model (R^2 >0.998 for PGBpy; >0.995 for PGBD), indicating uniform, single-layer adsorption on specific binding sites within the COF. This behavior is attributed to the heteroatom-rich pore environment, where protonated amine ($-NH^+$) and oxygen (–O– or –OH) sites under acidic conditions selectively bind $[AuCl_4]^-$ *via* electrostatic interactions and coordination bonding, as observed in adsorption experiments. The maximum adsorption capacity (Q_m) of PGBpy and PGBD was found to be 3467 mg g^{-1} and 2590 mg g^{-1}, respectively. The large Q_m value observed for PGBpy signifies the crucial role played by secondary coordination sites present in the COF backbone, inherited from Bpy unit in addition to the benzoxazine core. On the other hand, this was not the case for PGBD, due to the absence of an additional coordination site, which completely contributes to the heteroatom skeleton in the backbone. This controlled study has helped us to evaluate the role of additional nitrogen atoms present within the PGBpy in enhanced gold adsorption performance.

Since practical gold capture applications are often performed under acidic conditions, the adsorbent chemical stability while maintaining high uptake efficiencies becomes crucial. Considering this fact, we investigated the adsorption performance of COFs across a range of pH conditions, specifically between pH 2 and 12 (Fig. 2c). The findings demonstrated ~100% gold adsorption within the acidic pH range (2 to 6), where Au^{3+} primarily exists as planar $[AuCl_4]^-$ ions within the solution. Under acidic conditions, the protonated N_{amine} and O_{ether} functional groups within the COFs can efficiently adsorb $[AuCl_4]^-$ ions through electrostatic interactions.[32]

The selective uptake of gold ions over other competitive metal ions within the complex leaching solution is crucial for a real-life application. In this direction, for both COFs, we investigated selectivity by mimicking the metal composition of the real waste solution, including Au^{3+}, Cu^{2+}, Cr^{3+}, Al^{3+}, Zn^{2+}, Co^{2+}, and Cd^{2+} ions. According to our findings, PGBpy displayed excellent selectivity where the Au ions had a maximum uptake of 96.3% followed by the Cu^{2+} (6.2%), Cr^{3+} (4.2%), Al^{3+} (3.4%), Zn^{2+} (3.1%), Co^{2+} (2.1%), and Cd^{2+} (1.2%) (Fig. 2d). On the other hand, PGBD exhibited an uptake efficiency of 92.7% compared to Cu^{2+} (5.7%), Cr^{3+} (9.9%), Al^{3+} (2.2%), Zn^{2+} (3.7%), Co^{2+} (4.7%), and Cd^{2+} (2.0%). These observations suggest that the additional coordination sites (N_{Bpy}) in PGBpy played a crucial role in improving adsorption efficiency and selectivity. Meanwhile, PGBpy and PGBD demonstrated excellent distribution coefficient (K_d) values for gold ions compared to all the competing ions in the simulated e-waste (Table S9 and S11, ESI†). This outstanding performance can be primarily ascribed to the strategic incorporation of the benzoxazine core, which under acidic conditions (*e.g.*, pH 4–6), promotes the protonation of the amine ($-N \rightarrow -NH^+$) and partial protonation or hydrogen-bonding activation of oxygen sites which ultimately enhance the electrostatic attraction and coordination capability toward the anionic $[AuCl_4]^-$. This dual-protonation effect creates a highly polarized binding environment, amplifying the COF's affinity for gold ions beyond what single-site interactions typically achieve.

For the continuous adsorption of Au ions, the efficiency of the adsorbent for consecutive adsorption/desorption studies is critical.[33,34] In this direction, gold-adsorbed COFs were treated with the stripping solution (1 M thiourea and 1 M HCl) to regenerate and reuse the COFs for the next cycle of gold recovery. According to our investigation, both PGBpy and PGBD exhibit excellent gold uptake efficiency of >98% for ten and five consecutive adsorption/desorption cycles respectively (Fig. 2e and Fig. S29, ESI†). Meanwhile, there were no significant changes in the FTIR spectra of regenerated COFs compared to the pristine, suggesting the structural integrity remained intact even after multiple adsorption/desorption cycles (Fig. S31, ESI†).

3.3 Gold adsorbed COFs characterizations and DFT calculations

The gold-adsorbed benzoxazine COFs (*i.e.* Au@PGBpy and Au@PGBD) were characterized for the molecular-level understanding of the adsorption phenomenon. SEM and TEM studies were performed on Au@PGBpy and Au@PGBD samples to determine the morphological change (Fig. 2f–k and Fig. S12, Section S7, ESI†). SEM images exhibit no significant change in the sphere morphology of the COFs after adsorption of Au (Fig. S12, Section S7, ESI†). However, it is difficult to differentiate between the adsorbed gold nanoparticles and the COF matrix. In this aspect, TEM images (Fig. 2f and i) were recorded, affirming the agglomeration of gold nanoparticles on the sample's surface. Formations of gold nanoparticles suggest the *in situ* reduction of Au^{3+} ions to Au^0. This could be attributed to electron-rich N_{amine}, O_{ether}, and N_{Bpy} atoms in the COF backbone. Under acidic conditions, these heteroatoms get protonated and thus act as reducing sites for *in situ* reduction of Au^{3+} ions. HRTEM micrograph acquired for single gold nanoparticle at higher magnification in Au@PGBpy (Fig. 2g) and Au@PGBD (Fig. 2j) shows lattice fringes, which allow us to determine the lattice parameters. The *d*-spacing value of 0.23–0.25 nm corresponds to the (111) lattice plane of the gold was observed (Fig. 2h for Au@PGBpy and Fig. 2k for Au@PGBD). The average size of the gold particles was found to be 37.94 ± 0.53 nm for Au@PGBpy and 58.72 ± 0.72 nm for Au@PGBD (Fig. S33, Section S13, ESI†).

Furthermore, energy-dispersive X-ray (EDX) mapping performed on Au@PGBpy and Au@PGBD showed the uniform distribution of gold nanoparticles within the COF matrix (Fig. S34 and S35, Section S13, ESI†). After gold adsorption studies, the PXRD pattern of gold adsorbed COFs *i.e.* Au@COFs were recorded. In the PXRD pattern, the characteristic diffraction peaks of gold nanoparticles in Au@PGBpy and Au@PGBD samples dominate our as-synthesized COFs characteristic peaks, while simultaneously confirming the gold uptake (Fig. S24, ESI†). Whereas, the diffraction peaks present at $2\theta = 38.4°$ and $44.4°$ correspond to the diffraction from the 111 and 200 planes of Au^0 nanoparticle, respectively. To understand the interactions of gold nanoparticles with COFs, a full survey XPS profile analysis of Au@COFs was performed and compared with pristine samples (Fig. S15 and S16, Section S8, ESI†). For Au@PGBpy, the deconvolution of the high-resolution C 1s profile shows two discernible signals at 283.42 and 284.55 eV, signifying the C═C and C–C bonds of the PGBpy framework. In contrast, the broader signal appeared at 286.42 eV, which corresponds to the C–O/C–N bond. An observation of a slight shift in the binding energy value by ~0.78 eV for these C–O/C–N bonds to the higher value compared to pristine PGBpy indicates benzoxazine core interactions with $[AuCl_4]^-$. High-resolution N 1s spectra show three distinct peaks at 397.76, 398.78, and 399.68 eV, corresponding to C═N (Bpy), C–N, and Au–N, respectively, suggesting that the nitrogen sites present in the benzoxazine core and Bpy unit of the framework were participated for the Au adsorption (Fig. 3a). Two signals at 529.60 and 531.30 eV in the high-resolution O 1s spectra were attributed to C–O···Au and adventitious C–OH···Au bonds, respectively (Section S8, ESI†). Interestingly, compared to O 1s profile of pristine PGBpy, a significant shift of ~1.2–1.4 eV was observed for C–O–C and C–OH bond peaks. This observation suggests the presence of a strong interaction between the $O_{hydroxyl}$ and O_{ether} with the absorbed $[AuCl_4]^-$ ions.

In a high-resolution Au 4f XPS profile, peaks observed at 83.21 and 87.48 eV were assigned to the Au^0 $4f_{7/2}$ and Au^0 $4f_{5/2}$ states, respectively (Fig. 3c). Additionally, peaks at 83.99 and 89.37 eV correspond to the Au^{1+} $4f_{7/2}$ and Au^{1+} $4f_{5/2}$ states, while the peaks located at 85.43 and 91.39 eV are attributed to the

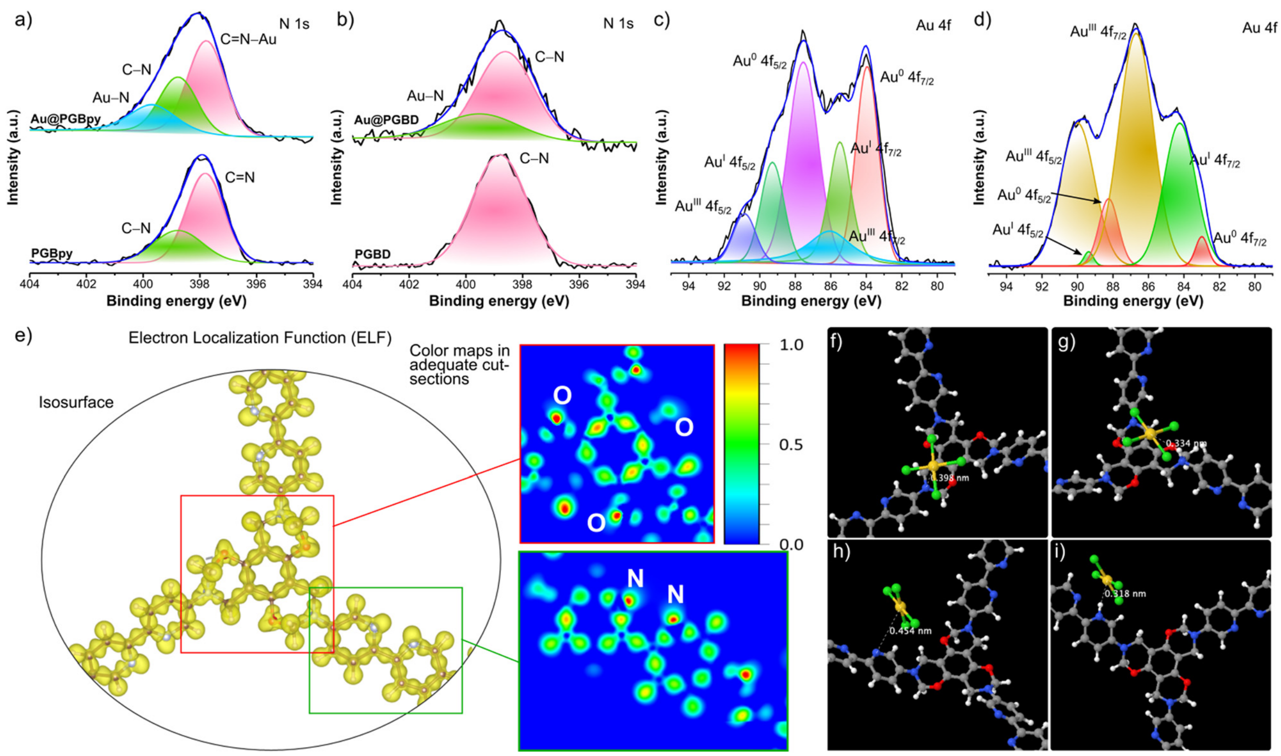

Fig. 3 A comparison of high-resolution N 1s XPS profile of (a) Au@PGBpy and (b) Au@PGBD with their respective pristine COFs. Au 4f XPS profile of (c) Au@PGBpy and (d) Au@PGBD. (e) Electron localization function (ELF) contour maps showing high electron density around O_{ether} (red box), and N_{amine} and N_{Bpy} atoms. PGBpy structure showing binding of $[AuCl_4]^-$ *via* interaction with N_{amine} in (f) unprotonated and (g) protonated state, and N_{Bpy} in (h) unprotonated and (i) protonated state.

Au^{3+} $4f_{7/2}$ and Au^{3+} $4f_{5/2}$ states. Au XPS profile analysis confirms the presence of Au^{3+} and its reduced form, Au^{1+} and Au^0, in the Au@PGBpy material. Notably, the high intensity of the Au^0 peaks, relative to those of Au^{3+} and Au^{1+} peaks, suggests that the reduction of Au^{3+} to Au^{1+} and Au^0 occurs instinctively upon the interaction of $[AuCl_4]^-$ with the benzoxazine core and Bpy unit of the framework. A similar analysis of Au@PGBD further validated the role of the benzoxazine core in providing binding sites for gold ions. A high-resolution C 1s profile displayed three peaks at 283.29, 284.51, and 286.94 eV corresponding to the C═C, C–C, and C–O/C–N bonds, respectively. Compared with the C 1s profile of PGBD, a slight shift of ∼0.6 eV in the binding energy of the C–O bond of Au@PGBD suggests that the O atom of the benzoxazine core is involved in interaction with gold ions. Meanwhile, a new peak at the binding energy value of 399.58 eV corresponds to Au–N_{amine} interaction as observed in the high resolution of N 1s for the Au@PGBD, compared with PGBD (Fig. 3b). The high-resolution O 1s profile displays two peaks at 530.64 and 532.49 eV, respectively. The peak at 530.64 eV corresponds to the binding energy of Au–O_{ether} interactions. A shift of ∼0.2 eV for the C–O_{ether} bond w.r.t. the O 1s profile of pristine PGBD suggests the involvement of the O atom of the benzoxazine core in gold adsorption. Furthermore, the 82.99 and 88.24 eV peaks were assigned to Au^0 $4f_{7/2}$ and Au^0 $4f_{5/2}$ states (Fig. 3d). On the other hand, the peaks present at 84.23 and 89.37 eV correspond to Au^{1+} $4f_{7/2}$ and Au^{1+} $4f_{5/2}$ states, while the peaks located at 86.70 and 90.03 eV correspond to Au^{3+} $4f_{7/2}$ and Au^{3+} $4f_{5/2}$ states. Au XPS profile suggests the majority of the gold absorbed from the feed solution is present in Au^{3+} form compared to its reduced form Au^{1+} and Au^0 in the Au@PGBD. In summary, we can conclude from XPS analysis that in the case of PGBpy, the Bpy serves as an additional site for reducing adsorbed Au^{3+} to the Au^0 state. Conversely, most of the gold ions adsorbed by the PGBD matrix are retained in the Au^{3+} state due to the absence of supplementary sites, which ultimately causes to lower the adsorption efficiency, compared to PGBpy. It is important to note that the N_{amine} and N_{Bpy} atoms present in these COFs can undergo protonation under acidic conditions and thus act as a reduction center for reducing Au^{3+} species to Au^{1+} and Au^0 species.

This is also validated by the fact that in nitrogen-rich PGBpy, we have observed a greater extent of Au^{3+} reduction into Au^0. To further support our proposed hypothesis and understand the mechanism of gold adsorption, the localization of electronic density in the COF skeleton was investigated using the DFT-based electron localization function (ELF) maps (Fig. 3e). The ELF map shows that O_{ether}, N_{amine}, and N_{Bpy} atoms are potential electron-donating sites for proton binding. Considering the presence of abundant O and N atoms within the COFs, we have estimated the binding energies for $[AuCl_4]^-$ adsorption on O and N atoms (before and after protonation) in the representative PGBpy (Fig. 3f and h). The binding energies on protonated N_{amine}, N_{Bpy}, and O_{ether} were found to be −5.31 (Fig. 3g), −3.93 (Fig. 3i), and −4.23 eV (Fig. S37a, Section S13, ESI†). On the other hand, the direct adsorption of $[AuCl_4]^-$ on the neutral COF structure showed unfavorable binding energy values of −1.44 for N_{amine} (Fig. 3f), −1.39 for N_{Bpy} (Fig. 3g), and −1.63 eV for O_{ether} (Fig. S37b, Section S13, ESI†). These findings suggest that the adsorption process begins with the protonation of active sites, which are subsequently attacked by H^+ ions from $[AuCl_4]^-$. These protonated active sites act as reducing centers, thus facilitating the formation of an intermediate $[AuCl_3]^-$ species by removing Cl^- from $[AuCl_4]^-$ accompanied by the generation of HCl molecules. Subsequently, the $[AuCl_3]^-$ binds to another protonated active site and is further reduced to $[AuCl_2]^-$. This reduction process sequentially continues step-by-step till Au^{3+} ions are reduced to Au^{1+} and Au^0 during adsorption. Importantly, the key step for Au^{3+} adsorption is the protonation of the active sites in our prepared COFs. This is further supported by the pH-dependent studies where the uptake efficiency of our prepared COFs is >99% while only <10% uptake efficiency in alkaline solution was observed (Fig. 2b). We want to highlight here that under acidic conditions, the protonation of the O_{ether} atom can induce the partial cleavage of the ring, resulting in the formation of a hydroxyl group that can interact with $[AuCl_4]^-$ more effectively, as suggested by the shift in the BE value observed in the high-resolution O 1s XPS profile of Au@PGBpy (Fig. S37b, Section S13, ESI†). However, in our case, FTIR studies show the benzoxazine core remains intact, which is confirmed by the absence of –OH stretch for Au@PGBpy (Fig. S23, Section S11, ESI†).

3.4 Gold adsorption using real e-waste

Towards our aim in the selective gold recovery from e-waste, a leaching solution was prepared by dissolving the discarded central processing unit (CPU) in aqua-regia for one day (Section S3, Fig. S36, ESI†). Other than gold, the leachate consists of Ag^{1+}, Pb^{2+}, Ni^{2+}, Cu^{2+}, Zn^{2+}, Al^{3+}, Ca^{2+}, $V^{3+/5+}$, Cr^{3+}, Mn^{3+}, Fe^{3+}, and Co^{2+} ions as determined from ICP-MS analysis (Fig. 4a and Fig. S30, Section S12, ESI†). Our investigation revealed that PGBpy and PGBD achieved maximum gold ion uptake efficiencies of 98.6% and 92.1%, respectively, with remarkable selectivity over the other competitive metal ions. Despite the presence of Ni^{2+}, Al^{3+}, Fe^{3+}, and Cu^{2+} ions in comparatively higher concentrations than Au^{3+}, the synthesized COFs displayed a strong affinity for Au^{3+} with a K_d value of 137.86 L g^{-1} and 23.27 L g^{-1} for PGBpy and PGBD respectively, demonstrating their superior selective adsorption (Fig. 4b and Table S10 and S12, ESI†). The observation of selective adsorption of Au^{3+} ion over other competing metal ions was further supported by the ion adsorption energies and kinetic modelling under acidic conditions performed by DFT calculations (Section S14, ESI†). From the thorough investigation of reported literature specifically for COFs in the quantitative adsorption of gold at room temperature, we found that both materials possess desirable adsorption capacities (Fig. 4c and Table S13, ESI†). Additionally, PGBD and PGBpy exhibit superior performance compared to the reported COF materials for gold recovery from real e-waste, considering their selective uptake efficiencies and the complexity of interfering ions (Fig. 4d). The superior selectivity

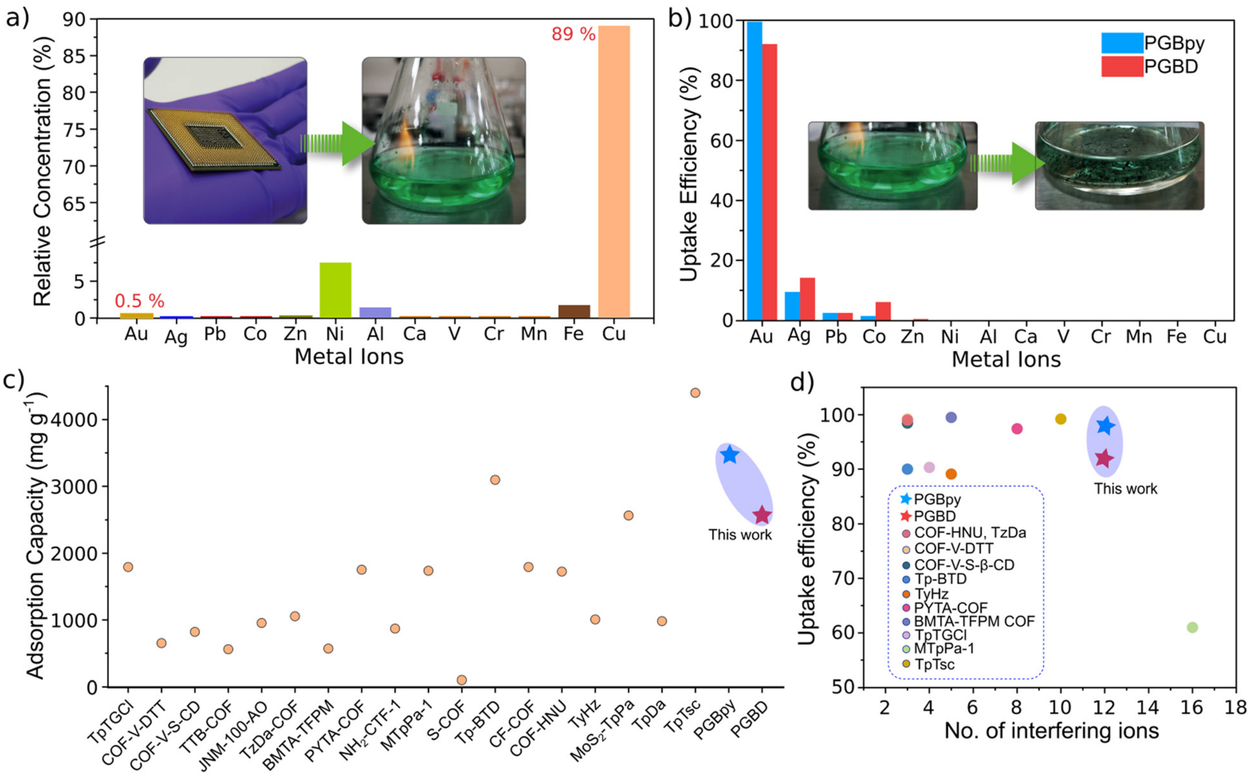

Fig. 4 (a) Relative concentration of constituent metal ions present in the e-waste leach solution, (b) uptake efficiencies of benzoxazine based-COFs corresponds to each metal ion from e-waste, (c) literature comparison w.r.t the adsorption capacities of different COFs reported for gold uptake and (d) Comparison of reported COF performance in gold uptake using real e-waste leach solution in terms of uptake efficiency and number of interfering ions considered for the study.

of Au ions towards the benzoxazine-based-COF can be due to its ability to get reduced into nanoparticles spontaneously compared to the other metal ions irrespective of being in very high concentration.

4. Conclusions

In conclusion, we synthesized quasi-planar benzoxazine-core COFs with tunable heteroatom distribution, specifically designed for gold recovery from e-waste. These COFs feature abundant nitrogen and oxygen sites within their pore interiors, enabling efficient gold uptake. BET surface area, though modest, remains sufficient to support ion diffusion, while the heteroatom-rich pore interior enhances adsorption capacity and selectivity—key metrics for our intended application. Through the protonation of nitrogen atoms in both the core and linkages, the COFs exhibited remarkable gold capture capacity and rapid adsorption kinetics. PGBpy achieved a maximum gold capture capacity of 3467 mg g^{-1}, reaching over 98% of its adsorption potential. Experimental data and theoretical calculations reveal that protonation of both imine and oxygen sites in PGBpy significantly enhances the binding affinity for $[AuCl_4]^-$, thereby accelerating the gold adsorption process. Moreover, both COFs selectively absorbed gold ($>$92%) over other competing metal ions commonly present in electronic waste. This study provides valuable insights into the design and functionalization of COFs, broadening their potential applications across various fields.

Author contributions

Sushil Kumar: conceptualization, data curation, formal analysis, investigation, methodology, validation, visualization, writing – original draft, review and editing. Mahira Bashri: data curation, formal analysis, investigation, writing – original draft, review and editing. Jose I. Martinez: DFT calculations, writing original theoretical draft, review & editing, theoretical findings. Matthew J. O'Connor: ICP-MS analysis, reviewing original manuscript draft. Sabu Varghese: solid-state NMR analysis, reviewing original manuscript draft. Blaz Belec: gas adsorption measurements, reviewing original manuscript draft. Gisha Elizabeth Luckachan: solid-state NMR analysis, reviewing original manuscript draft. Dinesh Shetty: conceptualization, writing – review & editing, supervision, resources, project administration, funding acquisition.

Conflicts of interest

The authors declare that they have no known competing financial interests or personal relationships that could have appeared to influence the work reported in this paper.

Data availability

Data related to this work are presented in the main manuscript and the ESI.† Additional relevant data are available from the corresponding author upon reasonable request.

Acknowledgements

Sushil Kumar and Dinesh Shetty acknowledge Khalifa University of Science & Technology, Abu Dhabi (UAE) for the generous support of this research. Sushil Kumar acknowledges Safa Gaber for SEM and TEM data collection, Jose I Martinez for theoretical studies, Matthew J O'Connor for ICP analysis, Sabu Varghese and Gisha Elizabeth Luckachan for solid-state NMR studies, and Blaž Belec for BET studies. Core Technologies Platform (CTP) at New York University Abu Dhabi for the ICP and solid-state NMR instrumentation. Dinesh Shetty acknowledges the financial support from the Khalifa University Competitive Internal Research Award (CIRA-2021) and resource support under the Center for Catalysis and Separations (CeCaS, grantRCII-2018-024). Mahira Bashri and Safa Gaber acknowledge Khalifa University of Science & Technology for PhD fellowship. José I Martínez acknowledges MICIU funding (Grants PID2023-149077OB-C31, TED2021-12941A-I00 and PLEC2021-007906 funded by MCIN/AEI/10.13039/501100011033 and by the 'European Union Next GenerationEU/PRTR'), and CAM (Grants FOTOSURF-CM: Y2020/NMT-6469, SYNMOLMAT-CM: TEC-2024/TEC-459). Blaž Belec acknowledges ARIS P2-0412 programme.

References

1 Global E-waste monitor 2024, https://www.globalewaste.org.
2 A. Balfourier, J. Kolosnjaj-Tabi, N. Luciani, F. Carn and F. Gazeau, *Proc. Natl. Acad. Sci. U. S. A.*, 2020, **117**, 22639–22648.
3 L. Yao, D. Bojic and M. Liu, *J. Pharm. Anal.*, 2023, **13**, 960–967.
4 J. Li, Y. Li, H. Liu and F. Ran, *Nano Energy*, 2024, **128**, 109839.
5 S. B. Ambegave, Shubham, T. R. More and N. T. Patil, *Chem. Commun.*, 2023, **59**, 8007–8016.
6 E. Falletta, M. Rossi and C. Della Pina, *Inorg. Chim. Acta*, 2022, **537**, 120959.
7 Y. R. Jeong, S. Y. Oh, J. W. Kim, S. W. Jin and J. S. Ha, *Chem. Eng. J.*, 2020, **384**, 123336.
8 Y. Sun, X. Fan, F. Liu, S. Li, J. Chen and S. Liu, *Mater. Lett.*, 2024, **365**, 136459.
9 L. Zhao, Q. Zhou, Y. Yang, Y. Zhang, Y. Qiu, Y. Chen, X. Jin, X. Yang and S. Wang, *J. Water Process Eng.*, 2024, **57**, 104572.
10 M. Ahmad, T. Shah, M. R. Tariq, L. Zhang, Y. Lyu, W. Iqbal, M. ud-din Naik, A. Khosla, Q. Zhang and B. Zhang, *J. Cleaner Prod.*, 2023, **426**, 139012.
11 J. K. Bediako, J.-W. Choi, M.-H. Song, Y. Zhao, S. Lin, A. K. Sarkar, C.-W. Cho and Y.-S. Yun, *Waste Manage.*, 2020, **113**, 225–235.
12 E. Moosavi-Khoonsari and N. Tripathi, *Processes*, 2024, **12**, 2795.
13 S. B. M K, Y.-S. Yun and S. Kancharla, *Coord. Chem. Rev.*, 2024, **507**, 215699.
14 A. F. M. Nogueira, A. R. F. Carreira, S. J. R. Vargas, H. Passos, N. Schaeffer and J. A. P. Coutinho, *Sep. Purif. Technol.*, 2023, **316**, 123797.
15 M. D. Rao, K. K. Singh, C. A. Morrison and J. B. Love, *Sep. Purif. Technol.*, 2021, **263**, 118400.
16 Y. He, M. Kiehbadroudinezhad, H. Hosseinzadeh-Bandbafha, V. K. Gupta, W. Peng, S. S. Lam, M. Tabatabaei and M. Aghbashlo, *Environ. Pollut.*, 2024, **342**, 123081.
17 L. V. Quispe-Garrido, J. G. Ruiz-Montoya, A. M. Baena-Moncada and A. La Rosa-Toro, *J. Environ. Chem. Eng.*, 2024, **12**, 112585.
18 S. Abubakar, G. Das, T. Prakasam, A. Jrad, F. Gándara, S. Varghese, T. Delclos, M. A. Olson and A. Trabolsi, *ACS Appl. Mater. Interfaces*, 2025, **17**, 17794–17803.
19 C. A. Fleming, A. Mezei, E. Bourricaudy, M. Canizares and M. Ashbury, *Minerals Eng.*, 2011, **24**, 484–494.
20 S. Wang, H. Wang, S. Wang, L. Zhang and L. Fu, *Microporous Mesoporous Mater.*, 2022, **341**, 112074.
21 C. S. Diercks and O. M. Yaghi, *Science*, 2017, **355**, eaal1585.
22 W. Guo, J. Liu, H. Tao, J. Meng, J. Yang, Q. Shuai, Y. Asakura, L. Huang and Y. Yamauchi, *Adv. Mater.*, 2024, **36**, 2405399.
23 M. Liu, D. Jiang, Y. Fu, G. Zheng Chen, S. Bi, X. Ding, J. He, B.-H. Han, Q. Xu and G. Zeng, *Angew. Chem., Int. Ed.*, 2024, **63**, e202317015.
24 D. Majumder, S. Fajal, M. M. Shirolkar, A. Torris, Y. Banyla, K. Biswas, S. Rasaily and S. K. Ghosh, *Angew. Chem., Int. Ed.*, 2024, e202419830.
25 Q. Guan, L.-L. Zhou and Y.-B. Dong, *J. Am. Chem. Soc.*, 2023, **145**, 1475–1496.
26 S. Wang, W.-C. Li, G.-P. Hao, Y. Hao, Q. Sun, X.-Q. Zhang and A.-H. Lu, *J. Am. Chem. Soc.*, 2011, **133**, 15304–15307.
27 S. Xu, J. He, S. Jin and B. Tan, *J. Colloid Interface Sci.*, 2018, **509**, 457–462.
28 C. H. M. Beraldo, M. R. da S. Silveira, A. F. Baldissera and C. A. Ferreira, *Prog. Org. Coat.*, 2019, **137**, 105321.
29 Y. Zhu, J. Su, R. Lin and P. Li, *Macromol. Res.*, 2020, **28**, 472–479.
30 C. Cheng, Y. Liu, G. Sheng, X. Jiang, X. Kang, C. Jiang, Y. Liu, Y. Zhu and Y. Cui, *Angew. Chem., Int. Ed.*, 2024, **63**, e202403473.
31 E. L. Spitler, B. T. Koo, J. L. Novotney, J. W. Colson, F. J. Uribe-Romo, G. D. Gutierrez, P. Clancy and W. R. Dichtel, *J. Am. Chem. Soc.*, 2011, **133**, 19416–19421.
32 T. Ma, R. Zhao, Z. Li, X. Jing, M. Faheem, J. Song, Y. Tian, X. Lv, Q. Shu and G. Zhu, *ACS Appl. Mater. Interfaces*, 2020, **12**, 30474–30482.
33 S. Yang, T. Li, Y. Cheng, W. Fan, L. Wang, Y. Liu, L. Bian, C.-H. Zhou, L.-Y. Zheng and Q.-E. Cao, *ACS Sustainable Chem. Eng.*, 2022, **10**, 9719–9731.
34 S. Zhong, Y. Wang, T. Bo, J. Lan, Z. Zhang, L. Sheng, J. Peng, L. Zhao, L. Yuan, M. Zhai and W. Shi, *Chem. Eng. J.*, 2023, **455**, 140523.